Suplementary information of „Molecular Organization in Polar Nematic Phases: A Combined FTIR Spectroscopy and Molecular Simulation Approach"

S1. Force Field Parameterization and Potential Energy Surface (PES) Validation

To accurately capture the conformational flexibility of the mesogenic core and mitigate the finite-size effects often observed in highly ordered liquid-crystalline phases, the default General Amber Force Field (GAFF) torsional parameters were refined. Following the Liquid Crystal Force Field (LCFF) methodology, we performed Potential Energy Surface (PES) scans using Density Functional Theory (DFT) at the B3LYP/6-311+G(d,p) GD3BJ level.

To ensure unambiguous assignment of the derived torsional parameters to specific linkages within the mesogenic core, **Scheme S1** illustrates the optimized molecular geometry alongside the explicit atom numbering convention. These atomic indices map directly to the implemented GROMACS topology and serve as the definitive structural reference for the dihedral definitions detailed in **Tables S1 and S2**.

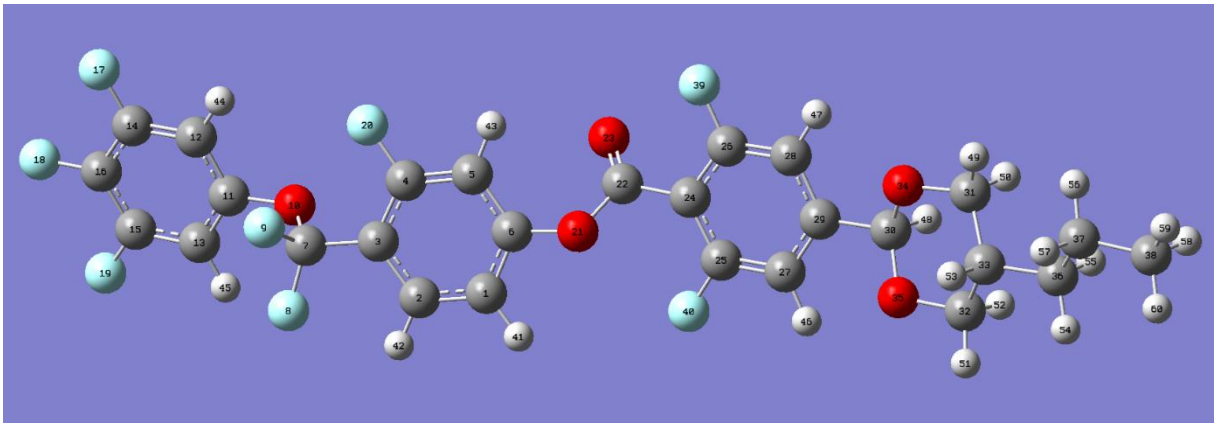

Scheme S1. Molecular structure and atom numbering scheme of the simulated mesogen, serving as the topological reference for the customized LCFF parameters.

During the fitting process, we observed that while standard Ryckaert-Bellemans (RB) polynomials (GROMACS funct 3) are sufficient for symmetric dihedral profiles (such as alkyl chains), several inter-ring and bridge linkages within the liquid crystal core exhibit highly asymmetric PES profiles due to local steric hindrances. To physically capture these asymmetric energy wells and ensure a thermodynamically accurate distribution of conformers, Multi-Harmonic Fourier series parameters (GROMACS funct 9) were explicitly derived for these specific dihedrals. The fully derived rotational coefficients, along with their corresponding atom types and functional forms, are tabulated in Tables S1 and S2.

To demonstrate the improvement over the unoptimized force field, Figure S1 presents the PES validation plots for key torsional angles. The relative energy profiles generated by the unmodified GAFF baseline frequently predict unphysical minima or significantly overestimate rotational barriers. In contrast, the energies calculated using our derived LCFF coefficients gracefully trace the target DFT data, confirming that the MD simulations inherently reproduce the *ab initio* torsional phase space.

Table S1. Derived Multi-Harmonic Fourier series parameters for the modified GAFF (LCFF approach, GROMACS funct 9). The table specifies the atom types defining the dihedral angles and their corresponding energy coefficients and phase shifts.

Dihedral Angle	Atom Indices	Phase ϕs,1 [°] / k1	Phase ϕs,2 [°] / k2	Phase ϕs,3 [°] / k3
C19–C20–C21–H8	28-29-30-48	0 / 0.000	356.3 / 5.34	0.00 / 0.000
C5–C6–O2–C14	5-6-21-22	235.82 / 2.090	282.07 / 10.824	119.62 / 0.955
O2–C14–C15–C16	21-22-24-25	321.41 / 0.894	88.22 / 13.812	34.35 / 0.709
C15–C14–O2–C6	24-22-21-6	340.38 / 2.313	174.83 / 18.066	173.79 / 0.950
O1–C7–C3–C2	10-7-3-2	119.31 / 1.933	58.52 / 2.700	174.99 / 0.356
C9–C8–O1–C7	12-11-10-7	0.32 / 0.000	338.09 / 6.619	0.33 / 0.000
C3–C7–O1–C8	3-7-10-11	352.17 / 4.461	173.10 / 5.500	160.84 / 6.193

Table S2. Derived Ryckaert-Bellemans polynomial coefficients for the modified GAFF (LCFF approach, GROMACS funct 3). The table specifies the atom indices defining the dihedral angles and the Cn coefficients.

Dihedral Angle	Atom Indices	C0	C1	C2	C3	C4	C5
C19–C20–C21–H8	28-29-30-48	-0.107	0.369	9.645	-1.987	1.295	1.638
C5–C6–O2–C14	5-6-21-22	15.001	0.723	-17.907	-1.246	21.738	1.747
O2–C14–C15–C16	21-22-24-25	17.191	-0.329	-14.669	1.290	15.360	-1.439
C15–C14–O2–C6	24-22-21-6	39.534	-9.435	-35.718	9.089	-2.253	-1.075
O1–C7–C3–C2	10-7-3-2	3.586	0.213	1.551	-0.870	1.462	2.332
C9–C8–O1–C7	12-11-10-7	0.041	0.281	9.638	-0.056	3.753	-0.463
C3–C7–O1–C8	3-7-10-11	11.729	-19.982	-5.438	19.469	-3.223	-0.266

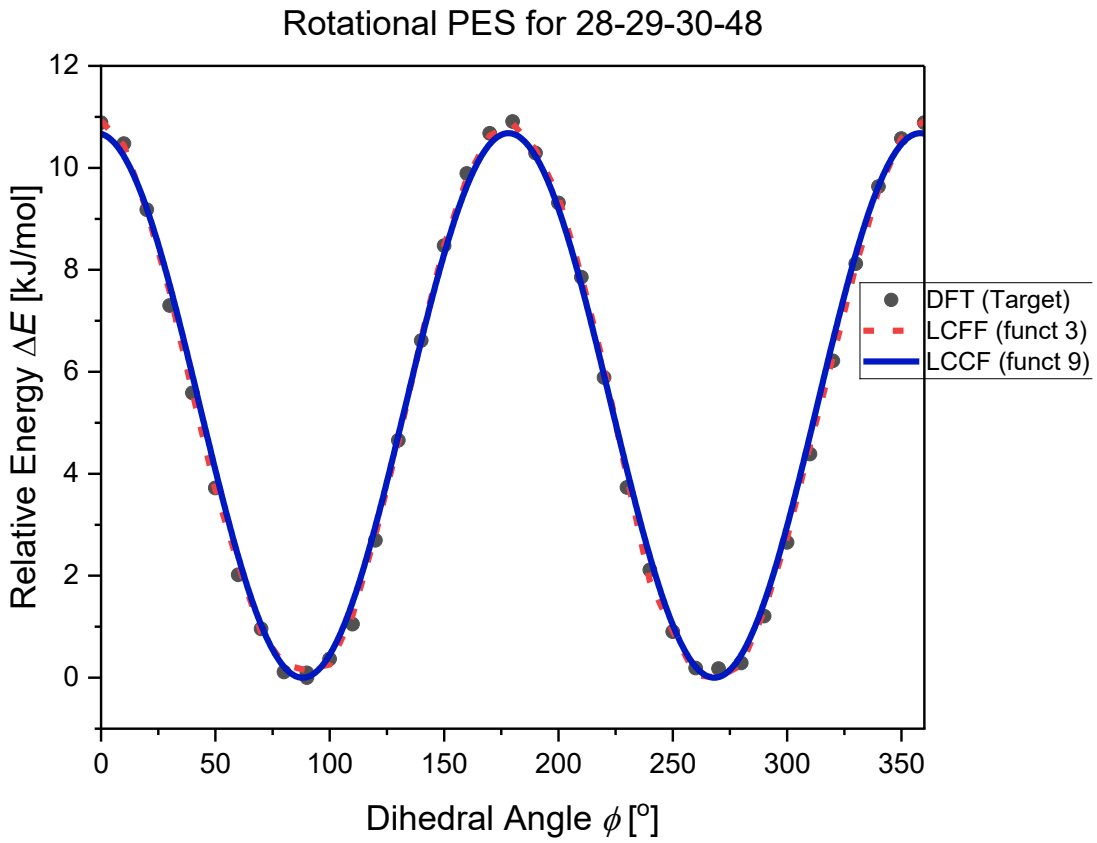

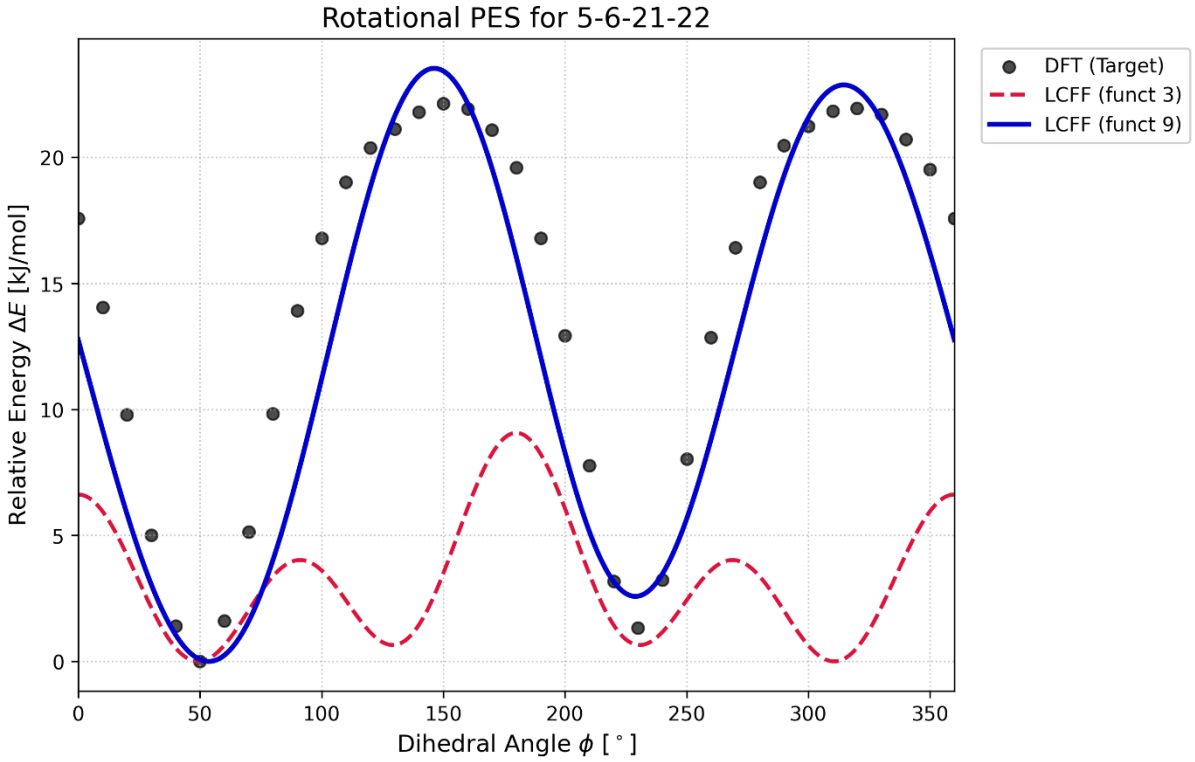
Rotational PES for 5-6-21-22
DFT (Target)
LCFF (funct 3)
LCFF (funct 9)
Relative Energy ΔE [kJ/mol]
Dihedral Angle ϕ [°]
0
5
10
15
20
0
50
100
150
200
250
300
350

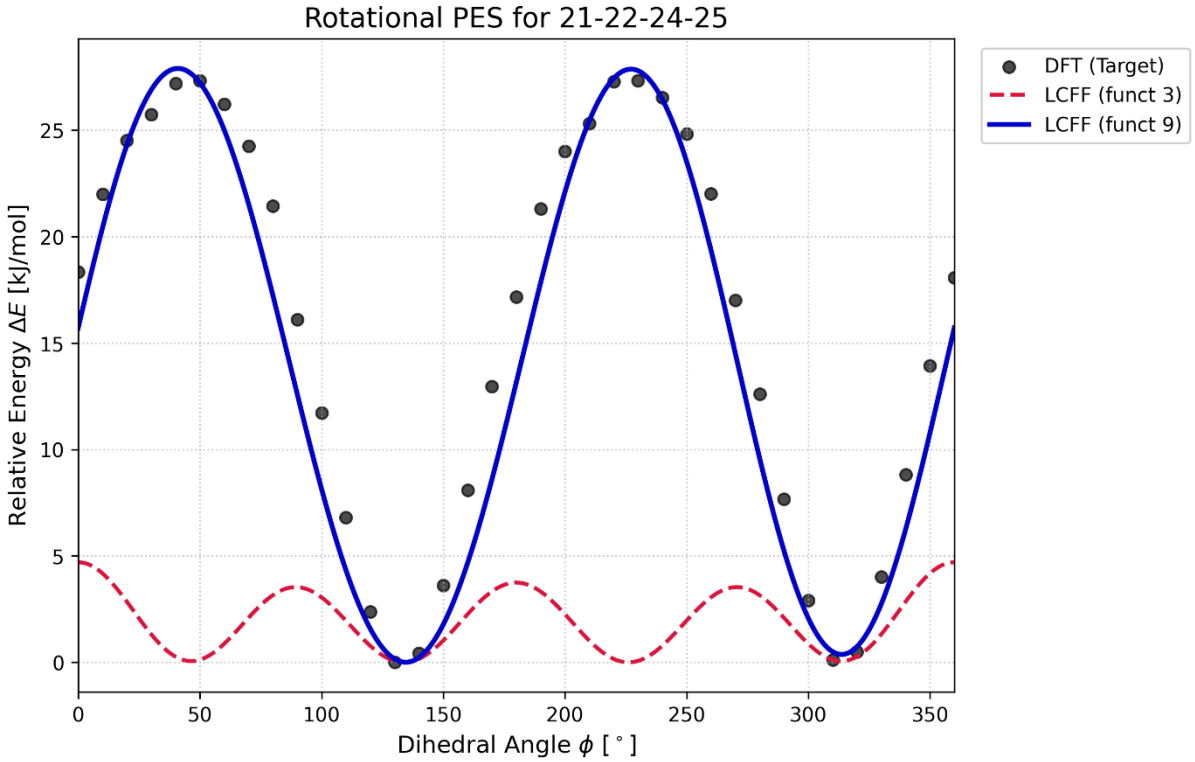
Rotational PES for 21-22-24-25
DFT (Target)
LCFF (funct 3)
LCFF (funct 9)
Relative Energy ΔE [kJ/mol]
Dihedral Angle ϕ [°]
0
5
10
15
20
25
0
50
100
150
200
250
300
350

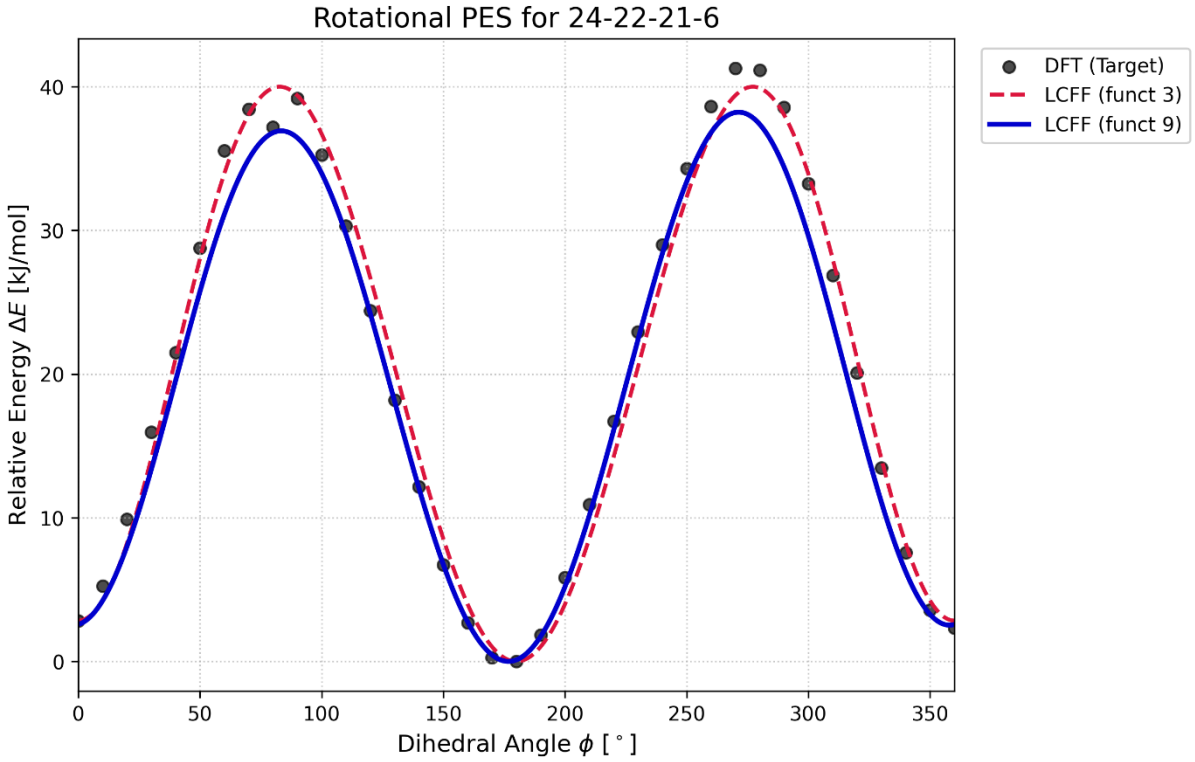
Rotational PES for 24-22-21-6
DFT (Target)
LCFF (funct 3)
LCFF (funct 9)
Relative Energy ΔE [kJ/mol]
Dihedral Angle ϕ [°]
0
10
20
30
40
0
50
100
150
200
250
300
350

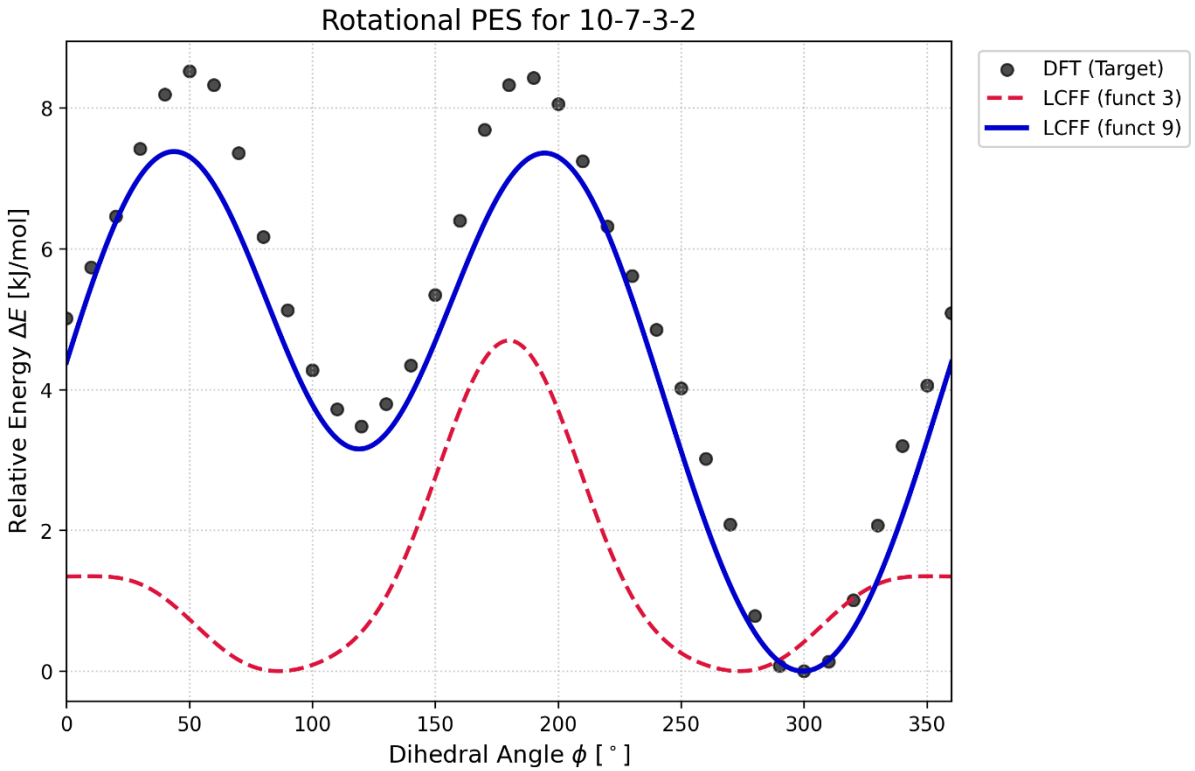
Rotational PES for 10-7-3-2
DFT (Target)
LCFF (funct 3)
LCFF (funct 9)
Relative Energy ΔE [kJ/mol]
Dihedral Angle ϕ [°]
0
2
4
6
8
0
50
100
150
200
250
300
350

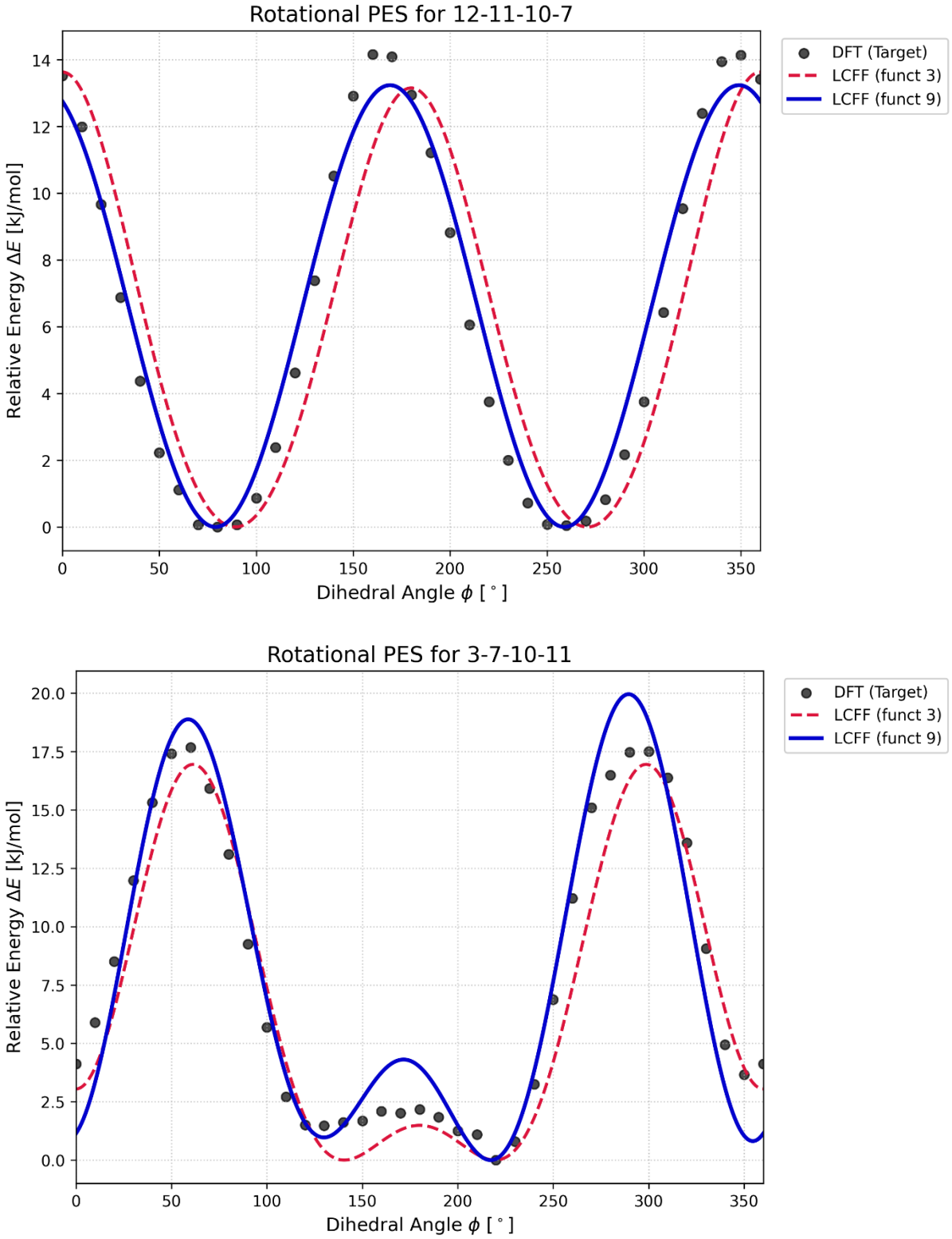

Figure S1. Potential Energy Surface (PES) validation for key dihedral angles of the 3JK molecule. Each plot compares the target DFT energy profile (black), the unoptimized GAFF baseline (red), and the profile generated by the newly derived rotational coefficients (blue).

S2. Long-term Stability of Orientational Order Parameters

A known issue with standard GAFF and anisotropic pressure coupling in ordered phases is the potential for dimensional collapse or artificial drift over time. To rigorously demonstrate the thermodynamic

stability of the simulated phases, the production runs were extended to 600 ns per temperature increment (100 ns initial equilibration + 500 ns extended production).

Figure S2 illustrates the temporal evolution of the nematic (P2) and polar (P1) order parameters for the simulated temperature range (340K – 380K). The plots confirm that after the initial equilibration phase, both order parameters reach a stable plateau and maintain it over hundreds of nanoseconds without any directional drift. Furthermore, the simulation box dimensions and macroscopic density remained strictly constant during these trajectories.

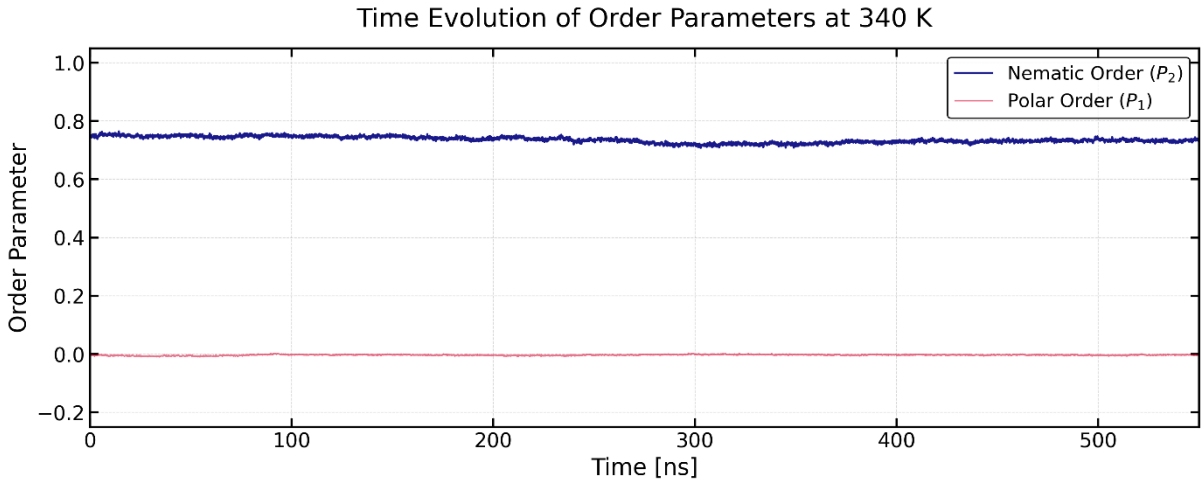

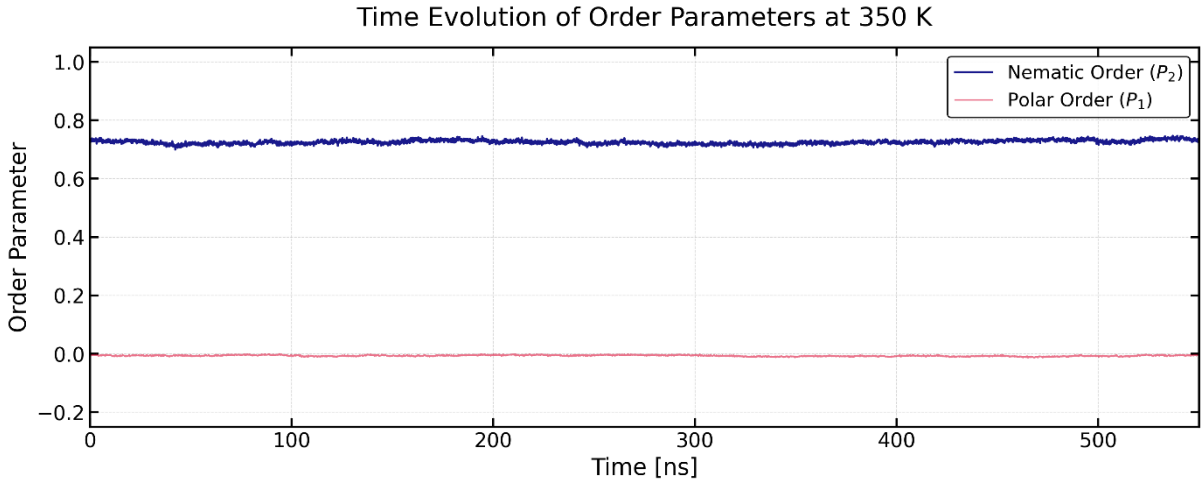

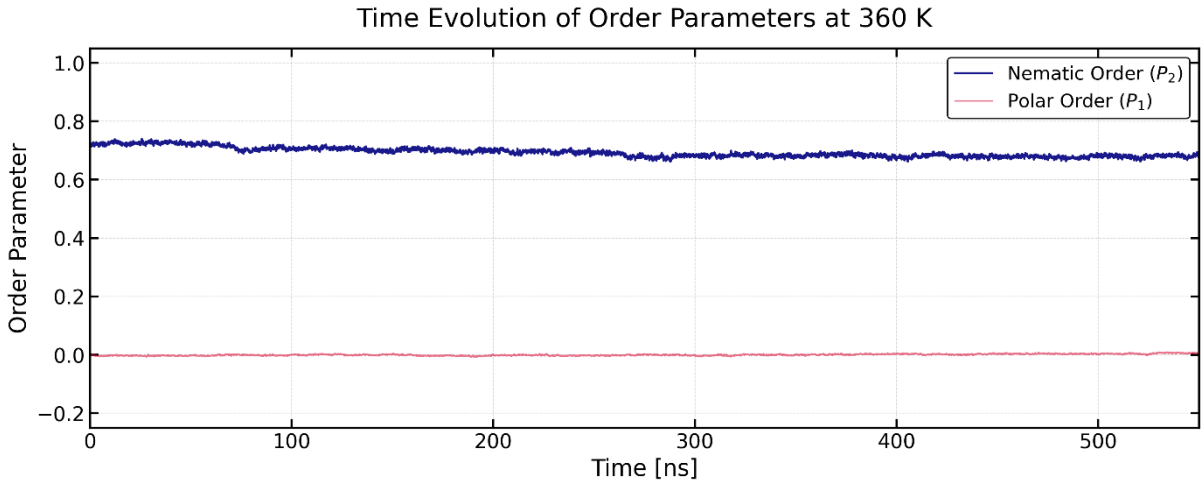

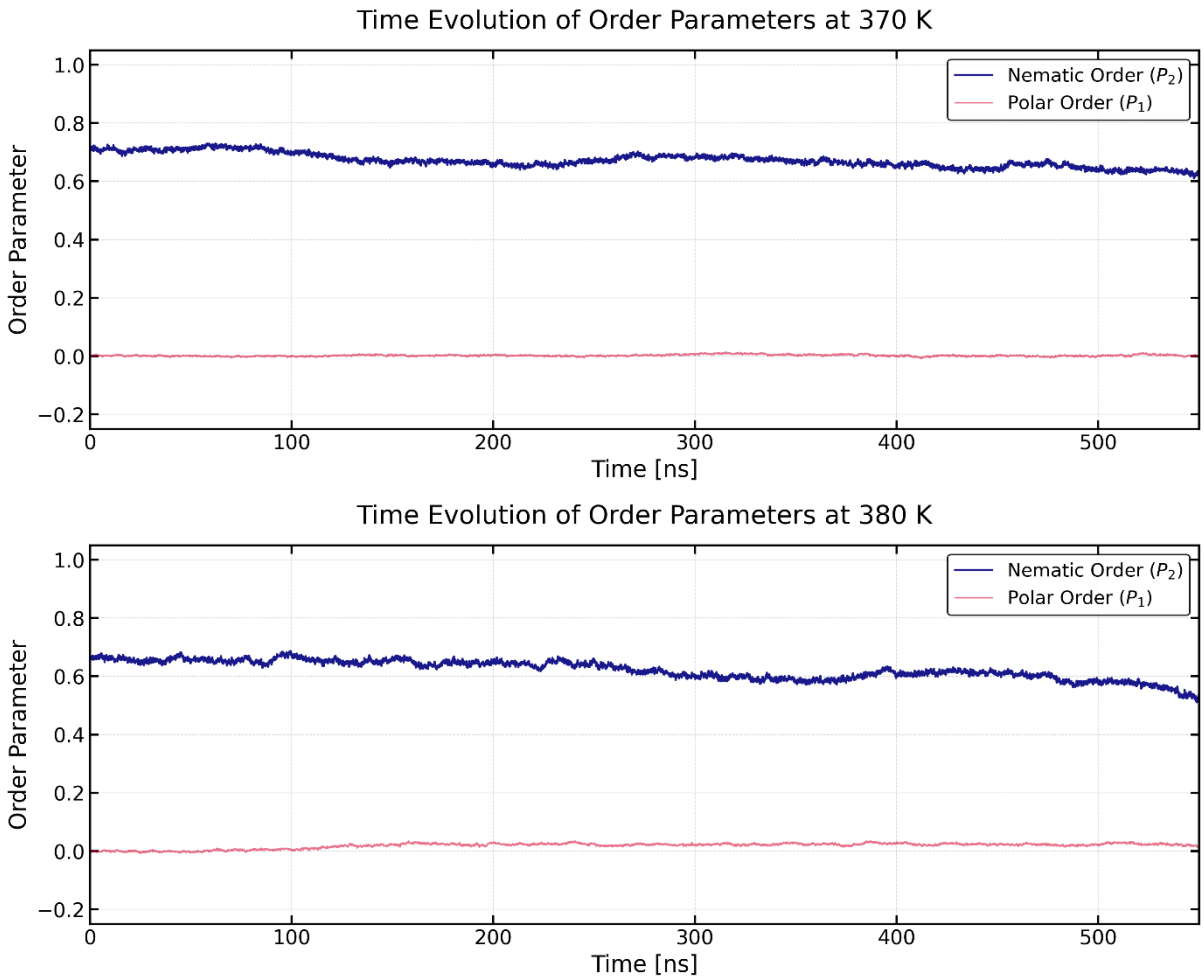

Figure S2. Time evolution of the nematic (P2, blue) and polar P1, red) order parameters over the full 600 ns continuous simulation time at representative temperatures: 340 K, 350 K, 360 K, 370 K, and 380K. The stable plateaus indicate full structural convergence.

S3. Spatial Organization and Temporal Evolution of Polar Nanodomains

To prove that these structures are a true thermodynamic feature rather than an artifact of the initial apolar setup, **Figure S3** tracks the temporal evolution of these domains. The 2D spatial polarization heatmaps demonstrate how local polar fluctuations grow, consolidate into distinct domains, and stabilize dynamically across the simulation timeline. This is further quantified by the distance-dependent polar spatial correlation function, g1(r) (discussed in the main text), which exhibits a definitive negative correlation at intermolecular distances of approximately 1.5 nm, proving the anti-parallel alignment of adjacent polar domains.

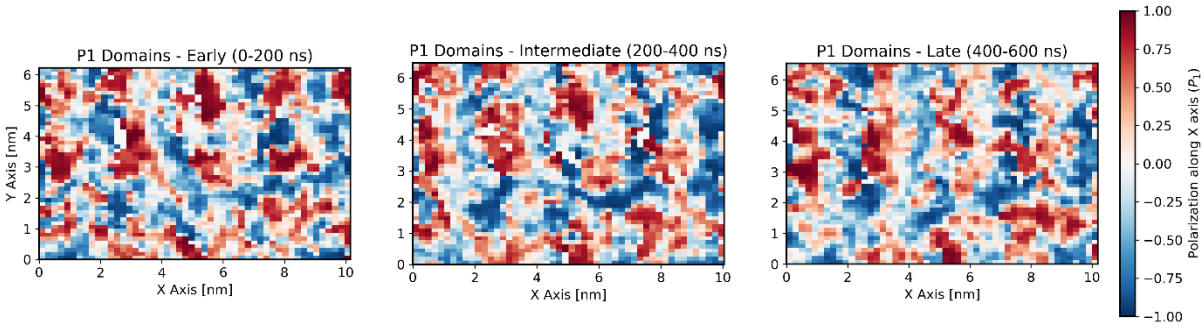

Figure S3. Spatiotemporal evolution of polar nanodomains. The 2D polarization heatmaps track the local polar order across the simulation box from early to late stages of the trajectory, illustrating the spontaneous growth, consolidation, and thermodynamic stability of the polar domains over time.